J Nanopart Res (2015) 17:286
DOI 10.1007/s11051-015-3090-6

RESEARCH PAPER

Factors influencing formation of highly dispersed $BaTiO_3$ nanospheres with uniform sizes in static hydrothermal synthesis

Jiabing Gao · Haiyue Shi · Huina Dong · Rui Zhang · Deliang Chen

Received: 12 September 2014 / Accepted: 23 June 2015 / Published online: 2 July 2015

Abstract Highly dispersed $BaTiO_3$ nanospheres with uniform sizes have important applications in micro/nanoscale functional devices. To achieve well-dispersed spherical $BaTiO_3$ nanocrystals, we carried out as reported in this paper the systematic investigation on the factors that influence the formation of $BaTiO_3$ nanospheres by the static hydrothermal process, including the NaOH concentrations [NaOH], molar Ba/Ti ratios ($R_{Ba/Ti}$), hydrothermal temperatures, and durations, with an emphasis on understanding the related mechanisms. Barium nitrate and TiO_2 sols derived from tetrabutyl titanate were used as the starting materials. The as-synthesized $BaTiO_3$ samples were characterized by X-ray diffraction, scanning electron microscopy, energy-dispersive X-ray analysis, thermogravimetry, differential thermal analysis, and FT-IR spectra. The highly dispersed $BaTiO_3$ nanospheres (76 ± 13 nm) were achieved under the optimum hydrothermal conditions at 200 °C for 10 h: [NaOH] = 2.0 mol L^{-1} and $R_{Ba/Ti} = 1.5$. Higher NaOH concentrations, higher Ba/Ti ratios, higher hydrothermal temperatures, and longer hydrothermal durations are favorable in forming $BaTiO_3$ nanospheres with larger fractions of tetragonal phase and higher yields; but too long hydrothermal durations resulted in abnormal growth and reduced the uniformity in particle sizes. The possible formation mechanisms for $BaTiO_3$ nanocrystals under the static hydrothermal conditions were investigated.

Keywords Barium titanate nanosphere · Static hydrothermal synthesis · Influencing factor · Formation mechanism

Introduction

Barium titanate ($BaTiO_3$) is one of typically important perovskite-structured materials, and has been widely used in ceramic condensers, high-density optical data storage, ultrasonic transducer, and piezoelectric devices (Koka and Sodano 2013; Masuda et al. 2008; Patel et al. 2012; Sahonta et al. 2011; Szwarcman et al. 2011). $BaTiO_3$, consisting of BaO_{12} cuboctahedra and TiO_6 octahedra, has three temperature-dependent phase transitions: (i) from rhombohedral (*R3m*) to orthorhombic (*Amm2*) at −90 °C, (ii) from orthorhombic to tetragonal (P4 mm) at 5 °C, and (iii) from tetragonal to cubic ($Pm\bar{3}m$) at 120 °C (Moreira and Microwave 2008). The three low-temperature phases (i.e., rhombohedral, orthorhombic, and tetragonal) are of a ferroelectric character,

Electronic supplementary material The online version of this article (doi:10.1007/s11051-015-3090-6) contains supplementary material, which is available to authorized users.

J. Gao · H. Shi · H. Dong · R. Zhang · D. Chen (✉)
School of Materials Science and Engineering, Zhengzhou University, 100 Science Road, Zhengzhou 450001, People's Republic of China
e-mail: dlchen@zzu.edu.cn

whereas the high-temperature phase (i.e., cubic) is para-electric (Bandura and Evarestov2012; Hwang et al. 2002; Kim et al. 2014). Recently, $BaTiO_3$-based perovskite-structured materials have attracted increasing attention in multilayer ceramic capacitors (MLCC), because of their high relative permittivity (ε_r) and low dielectric loss (Haertling 1999; Ouyang et al. 2010; Kimmel et al. 2013). To achieve miniaturization of electronic devices, novel capacitors with smaller volumes are the requisites. In order to shrink large-capacitance MLCCs, the engineers have to decrease the thickness of the MLCCs dielectric layers (Masuda et al. 2003), and therefore the $BaTiO_3$-based materials with smaller particle sizes and well-defined spherical morphology are needed (Stawski et al. 2012; Joung et al. 2011; Paniagua et al. 2014). When the thickness of the dielectric layers decreases to 0.5 μm, the sizes of the $BaTiO_3$ powders used should be controlled to be less than 100 nm, and tetragonal $BaTiO_3$ nanocrystals are needed (Shiratori et al. 2007; Xia et al. 1996). To achieve full control on the size, morphology, and phase of the $BaTiO_3$-based materials, scientists have to systematically understand effects of the factors that influence the morphologies, microstructures, and phases of $BaTiO_3$ nanocrystals (Xia et al. 1996; Bai et al. 2012; Hoshina et al. 2008).

Many processes have been developed to synthesize $BaTiO_3$ nanocrystals and their composites (Ko et al. 2013; Xie et al. 2010; Wang et al. 2006). The conventional methods for the fabrication of $BaTiO_3$ powders involve similar solid-state reactions of carbonates and oxides (i.e., $BaCO_3$ and TiO_2) at enhanced temperatures, but the particle sizes of the as-obtained products are large (micrometer level), and their morphologies cannot be effectively controlled (Tian et al. 2008). For the synthesis of pure and uniform-sized $BaTiO_3$ nanocrystals, the hydrothermal processes in various solvents at low temperatures are proven to be efficient, and the as-obtained nanocrystals are usually of a narrow particle-size distribution and well-controlled morphology (Xu and Gao 2002; Zhan et al. 2012; Pramanik et al. 2006; Badheka et al. 2006). Low reaction temperatures in hydrothermal processes can avoid the problems (such as poor stoichiometry) encountered with the high-temperature processes (i.e., solid-state reactions) due to easy volatilization of some components (Riman et al. 2002). However, the factors influencing the hydrothermal synthesis of $BaTiO_3$ nanocrystals are complex; for example, the formation rates and the yields of $BaTiO_3$ nanocrystals are considerably influenced by hydroxyl concentrations and pH values (Slamovich and Aksay 1994; Shin et al. 2014). Therefore, it is necessary to define empirically the fundamental effects of the parameters (i.e., reaction temperatures, pressures, and durations, precursor concentrations, and pH values) on the crystallization thermodynamics and kinetics of the growth of $BaTiO_3$ nanocrystals (Tian et al. 2008; Tang and Sodano 2013). For the wet-chemical growth of $BaTiO_3$ nanocrystals, there are three possible mechanisms proposed: (i) Ostwald ripening process (Zeng 2006), (ii) oriented attachment (Zhou 2010), and (iii) reversed crystal-growth mechanisms (Qi et al. 2011). Understanding the details for the hydrothermal growth mechanism is another essential requirement for the scale-up synthesis of $BaTiO_3$ nanocrystals with controlled sizes and morphologies. To the best of our knowledge, further simplification of the synthetic process, effective control over the microstructures and phases, and complete understanding of the influencing factors and the related formation mechanisms during the hydrothermal synthesis of $BaTiO_3$ nanocrystals are still to be realized and remain as challenges to overcome (Gajović et al. 2013; Zeng 2007; Shiratori et al. 2007).

In this work, we systematically investigate the major factors that influence the formation of $BaTiO_3$ nanocrystals using $Ba(NO_3)_2$ and TiO_2 sols as the model starting precursors during the static hydrothermal process. The relevant major factors include NaOH concentrations [NaOH], molar Ba/Ti ratios ($R_{Ba/Ti}$), hydrothermal temperatures, and durations, with emphases on the understanding the process–microstructure–phase relationships and their related mechanisms.

Materials and methods

Materials and chemicals

Tetrabutyl titanate ($Ti(OC_4H_9)_4$, TNB, analytically pure), and barium nitrate ($Ba(NO_3)_2$, chemically pure) were purchased from Sinopharm Chemical Reagent Co. Ltd.. Sodium hydrate (NaOH, analytically pure), glacial acetic acid ($C_2H_4O_2$, analytically pure),and isopropyl alcohol (C_3H_8O, analytically pure) were purchased from Tianjing Kermel Cheimcal Reagent Co. Ltd.. Ethanol (analytically pure) was purchased

from Anhui Ante Biochemical Co. Ltd.. All reagents were used as received without further purification. Distilled water was normally used in the experiments, unless specifically stated otherwise.

Synthesis of highly dispersed $BaTiO_3$ nanocrystals

The synthesis of the highly dispersed $BaTiO_3$ nanocrystals involved two steps: the preparation of TiO_2 sol and then the static hydrothermal treatment. For the preparation of TiO_2 sol, isopropyl alcohol (80 mL), and tetra-butyl titanate (80 mL) were first mixed to form a transparent solution, which was then dropwise added into the glacial acetic acid aqueous solution (30 mL of glacial acetic acid in 800 ml of distilled water) under vigorous magnetic stirring at room temperature. The above mixture obtained was kept under stirring for more than 3 days to form a translucent TiO_2 sol as a stock reactant for later use. For the synthesis of $BaTiO_3$ nanocrystals, a given amount of $Ba(NO_3)_2$ was first dissolved into 60 ml of the above TiO_2 sol according to the designed molar Ba/Ti ratio ($R_{Ba/Ti} = 0.7–2.0$); then NaOH solution (20 mL) with a given amount of NaOH solids was added to the Ba^{2+}–TiO_2 sol, and the NaOH concentration was kept in the range of 0.6–3.0 mol L^{-1} based on the total volume of 80 mL. With the addition of NaOH solutions, the above semitransparent Ba^{2+}–TiO_2 sols turned to milky-white precipitates, forming $Ba(OH)_2$ due to the reaction of Ba^{2+} ions with OH^- ions. After 30-min stirring, the milky-white precipitates were transferred to a Teflon-lined autoclave (100 mL in volume), which was then heated in the range of 100–200 °C for a duration of 10 min–100 h under a static hydrothermal condition. After the hydrothermal reaction, the autoclave was naturally cooled to room temperature. The lower part of the treated product appeared as white precipitates and the upper was in the form of transparent solutions. The white precipitates were collected by centrifugation, washed with de-ionized water, and ethanol several times, and then dried overnight at 60 °C.

Characterization and analysis

The phase compositions of the $BaTiO_3$ nanocrystals synthesized were determined by X-ray diffraction (XRD) performed on an XD-3 X-ray diffractometer (Beijing Purkinje General Instrument Co., Ltd., China) with Cu Kα irradiation ($\lambda = 0.15406$ nm). The morphologies and microstructures of the $BaTiO_3$ samples were observed using a field-emission electron scanning microscope (FE-SEM, JEOL 7500F), and a field-emission transmission electron microscope (FE-TEM, Tecnai G2F20, accelerating voltage of 200 kV, Philips) with an attachment of energy dispersive analysis of x-rays (EDAX). TG analyses were performed using a thermogravimetric analyzer TA Q50 (TA Instruments) under air atmosphere. The $BaTiO_3$ samples were heated from room temperature to 1000 °C at a rate of 10 °C min^{-1}. Fourier transformed infrared (FT-IR) spectra were recorded in wavenumbers ranging from 4000 to 400 cm^{-1} using a Bruker-Equinox 55 spectrometer in a transmittance mode. The particle-size distribution of the $BaTiO_3$ samples was statistically analyzed based on the SEM observations. The morphologies and microstructures of the samples were observed using a field-emission electron scanning microscope (FE-SEM, JEOL 7500F), and a field-emission transmission electron microscope (FE-TEM, Tecnai G^2 F20, accelerating voltage of 200 kV, Philips). Raman spectra were recorded in the 100–1000 cm^{-1} wavenumber range using a Horiba Xplora Raman microscope (Horiba Scientific).

Results and discussion

Synthesis and characterization of typical highly dispersed $BaTiO_3$ nanospheres

The formation of $BaTiO_3$ nanoparticles experienced nucleation of TiO_2 sols and then deposition of Ba^{2+} on TiO_2 nucleus in an alkaline solution under static hydrothermal conditions. Figure 1 shows the morphology and composition of the typical $BaTiO_3$ nanocrystals synthesized by hydrothermal treatment at 200 °C for 10 h with a [NaOH] of 2 mol L^{-1} and a molar Ba/Ti ratio ($R_{Ba/Ti}$) of 1.5. Figure 1a, b shows typical SEM images of the as-synthesized $BaTiO_3$ sample. The low-magnified SEM image (Fig. 1a) indicates that the sample consists of uniform, spherical $BaTiO_3$ particles. The corresponding high-magnified SEM image shows that the spherical particles are well separated, and their sizes are less than 100 nm. The

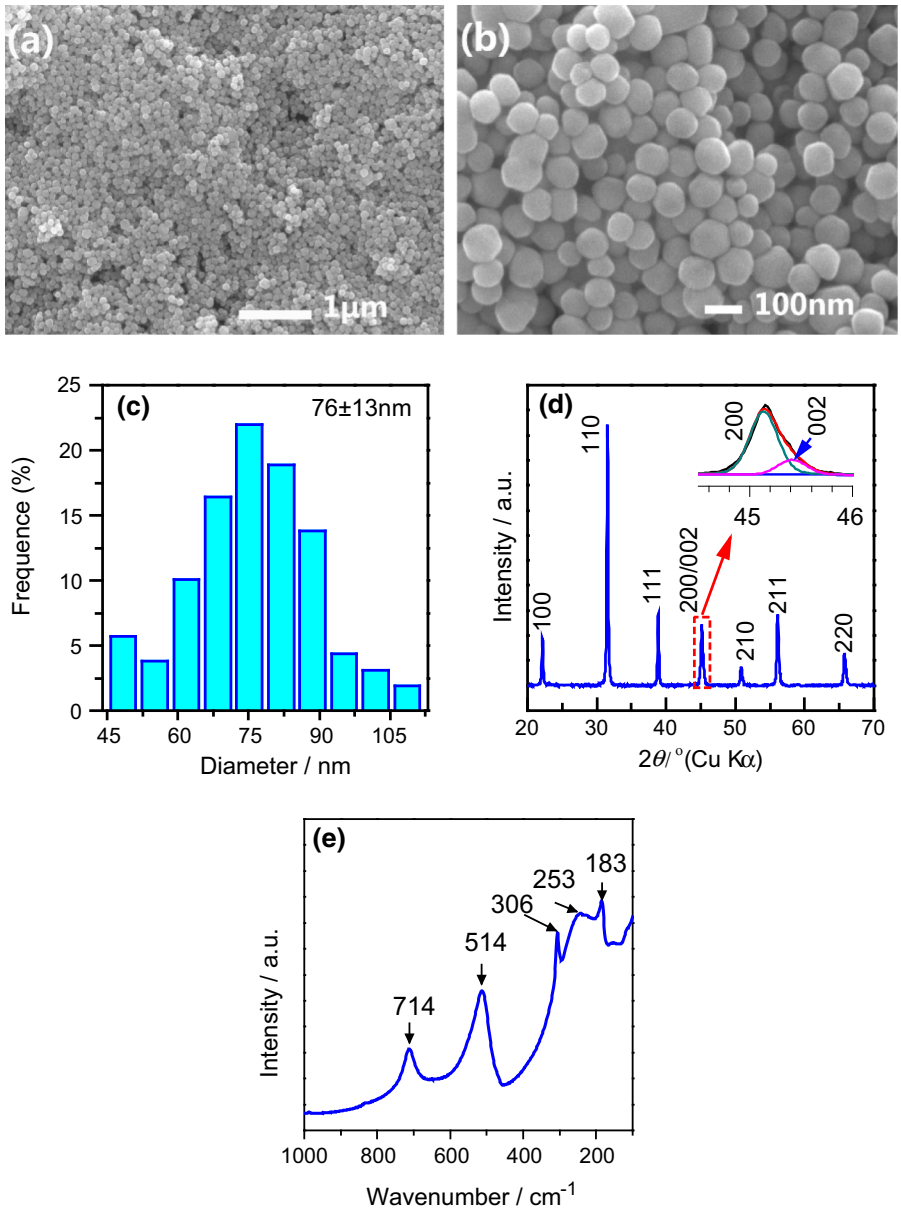

Fig. 1 **a**, **b** SEM images, **c** size-distribution histograms, **d** XRD patterns, and **e** Raman spectra of typical $BaTiO_3$ nanoparticles synthesized by a static hydrothermal process at 200 °C for 10 h ([NaOH] = 2.0 mol L^{-1}, and $R_{Ba/Ti} = 1.5$)

statistical analysis of the particle-size distribution based on the SEM observations is shown in Fig. 1c, and the average size is 76 ± 13 nm.

The XRD spectrum of the as-synthesized sample is shown in Fig. 1d. There are seven obvious peaks at around 22.12, 31.52, 38.81, 45.17, 50.80, 56.10, and 65.76°, corresponding to the (100), (110), (111), (200), (210), (211), and (220) reflections of the cubic $BaTiO_3$ phase, respectively, according to the literature (JCPDS card no. 31-0174) (Patel et al. 2012; Joung et al. 2011; Hoshina et al. 2008). The cell parameter which was calculated using the Cell Unit program was estimated to be $a = 0.40133(6)$ nm, very close to the literature data ($a = 0.4031$ nm, JCPDS card no. 31-0174) (Zhan et al. 2012). Actually, the diffraction peak at around 45° can be

split into two possible peaks located at 45.1° and 45.4°, with an intensity ratio ($I_{45.1}/I_{45.4}$) of 4.3. According to the standard data (JCPDS card no. 05-0626), the tetragonal $BaTiO_3$ has (200) and (002) reflections at 44.9° and 45.4°, respectively (Xie et al. 2010); whereas the cubic $BaTiO_3$ (JCPDS card no. 31-0174) shows the (200) reflection at ~45.0° (Masuda et al. 2008). The amount of tetragonal phase can be estimated according to the ratio of $I_{45.4}/(I_{45.4} + I_{45.1})$, where $I_{45.4}$ and $I_{45.1}$ are the peak intensities of tetragonal phase and cubic phase at 2θ values of around 45.4° and 45.1°, respectively. The calculated results are listed in Table S1. Therefore, the sample synthesized under the present conditions may be a mixture of cubic (JCPDS card no. 31-0174) and tetragonal (JCPDS card no. 05-0626) $BaTiO_3$ phases, and the amount of tetragonal phase is about 21.7 % according to the XRD data (Fig. 1d; Table S1).

Figure 1e shows the Raman spectra of the as-synthesized $BaTiO_3$ nanospheres. They are expected to have eight Raman active modes for tetragonal $BaTiO_3$ with a space group P4 mm, 3A1 g + B1 g + 4Eg (Masuda et al. 2008; Gajović et al.2013). The peaks at around 514, 253, and 183 cm^{-1} are assignable to the fundamental TO modes (transverse component of the optical mode) of the A1 symmetry, and the peak at ~306 cm^{-1} can be assigned to the B1 mode, indicating an asymmetry within the TiO_6 octahedra of $BaTiO_3$ on a local scale (Moreira and Microwave 2008; Gajović et al. 2013). The broad band at around 714 cm^{-1} should be related to the high-frequency longitudinal optical mode (LO) of A1 symmetry (Gajović et al. 2013). If the sharpness of the peak at 306 cm^{-1} is reduced or it becomes indistinct, the tetragonal phase is not dominant in the sample (Shiratori et al. 2007; Gajović et al. 2013; Shiratori et al. 2007). However, the Raman peak at 306 cm^{-1} of the present $BaTiO_3$ sample is sharp, indicating that the as-synthesized $BaTiO_3$ samples via hydrothermal treatment at 200 °C for 10 h consist of a large amount of tetragonal $BaTiO_3$ phase, in agreement with its XRD result (Fig. 1d).

Taking the SEM, XRD, and Raman spectra into account, the as-obtained $BaTiO_3$ sample mainly consists of highly dispersed $BaTiO_3$ nanospheres with nanoscale diameters (76 ± 13 nm) and mixed phase compositions (tetragonal and cubic), being suitable as functional inks for ink-jet printing devices.

Effects of NaOH concentrations

From the thermodynamic point of view, $BaTiO_3$ can be formed in a strong alkaline condition, because the solubility of barium titanate increases in low pH solutions (Un-Yeon et al. 2004). The formation reaction of $BaTiO_3$ can also occur at low pH solutions but only at an elevated temperature (Riman et al.2002). Until now, it is not very clear how to balance the alkalinity and temperature during the formation of $BaTiO_3$ nanocrystals. To investigate the effect of alkalinity on the crystallinity and morphology of the $BaTiO_3$ products, we synthesized a series of $BaTiO_3$ samples with various NaOH concentrations ([NaOH] ~0.6–3.0 mol L^{-1}), and the hydrothermal temperature, duration, and Ba/Ti ratio were kept the same values: 200 °C for 10 h with $R_{Ba/Ti} = 1.2$. The yields of $BaTiO_3$ solids increase with the increase in NaOH concentration, and the yield increases from ~70 % when [NaOH] is ~0.6–0.8 mol L^{-1} to over 90 % when [NaOH] is ~1.0–3.0 mol L^{-1}.

Figure 2 shows the typical XRD patterns of the $BaTiO_3$ samples synthesized with various NaOH concentrations at 200 °C for 10 h with a Ba/Ti ratio of 1.2. As the XRD patterns show (Fig. 2b–e), when the [NaOH] is not less than 0.8 mol L^{-1}, the as-synthesized samples have similar XRD patterns, which can be indexed to $BaTiO_3$ phases (tetragonal (JCPDF 05-0626) or cubic (JCPDF no. 31-0174)), and no impure phases can be found (Patel et al. 2012). When the NaOH concentration is too low, i.e., 0.6 mol L^{-1} (Fig. 2a), there are some diffraction peaks belonging to $BaCO_3$, besides the peaks belonging to the $BaTiO_3$ phases. Under low NaOH concentrations, the solubility of $BaTiO_3$ increases and the as-obtained Ba^{2+} ions can react with CO_2 dissolved in the solution to form $BaCO_3$ phase (Joung et al. 2011). As the broadened XRD patterns in the 2θ range of 44–46° (right in Fig. 2) show, the $BaTiO_3$ sample synthesized in a low [NaOH] of 0.6 mol L^{-1} has one diffraction peak at ~45.1°, very close to the (200) reflection (44.964°) of the cubic $BaTiO_3$ phase according to JCPDF no. 31-0174, indicating that the $BaTiO_3$ sample synthesized in a low [NaOH] concentration consists of a cubic phase(Masuda et al. 2008; Patel

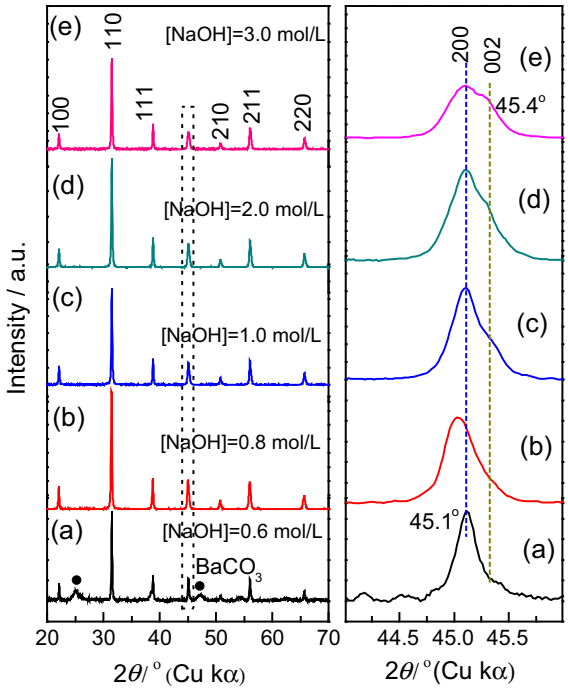

Fig. 2 Typical XRD patterns of $BaTiO_3$ samples obtained by static hydrothermal treatment at 200 °C for 10 h with $R_{Ba/Ti} = 1.2$ and various NaOH concentrations: *a* 0.6 mol L^{-1}, *b* 0.8 mol L^{-1}, *c* 1.0 mol L^{-1}, *d* 2.0 mol L^{-1}, and *e* 3.0 mol L^{-1}

et al. 2012). When the [NaOH] concentration increases from 0.6 to 3.0 mol L^{-1}, the diffraction peaks at around 45° of the as-synthesized $BaTiO_3$ samples can be split into two obvious sub-peaks, assignable to (200) and (002) reflections of the tetragonal $BaTiO_3$ phase. The splitting of the diffraction peaks around 2θ of 45° [(200) and (002)] is characteristic of the tetragonal $BaTiO_3$ phase. The amounts of the tetragonal $BaTiO_3$ phase can be estimated based on the XRD data (Fig. S1; Table S1), and the percentage of the tetragonal $BaTiO_3$ phase increases from 18 to 40 % with the increase of [NaOH] concentration from 0.6 to 3.0 mol L^{-1}. Therefore, we can conclude that the enhancements in NaOH concentrations in initial solutions are favorable in the formation of tetragonal $BaTiO_3$ phase.

Figure 3 shows the typical SEM images of the $BaTiO_3$ samples synthesized with different NaOH concentrations under static hydrothermal treatment at 200 °C for 10 h with a Ba/Ti ratio of 1.2. For the low [NaOH] cases (i.e., 0.6–0.8 mol L^{-1}), as shown in Fig. 3a and b, the $BaTiO_3$ samples obtained consist of large aggregates of small $BaTiO_3$ nanoparticles, which are unrecognizable in morphology and size of their primary particles. When the [NaOH] concentration increases to over 1.0 mol L^{-1}, the samples consist of definitely spherical and highly dispersed $BaTiO_3$ nanoparticles, as shown in Fig. 3c–e. Their particle-sizes are statistically analyzed based on the SEM observations, and shown in Fig. 3f. One can find that the sizes of the $BaTiO_3$ nanospheres synthesized at [NaOH] = 1.0 mol L^{-1} are 105 ± 21 nm, and the $BaTiO_3$ samples synthesized at [NaOH] = 2.0 mol L^{-1} and [NaOH] = 3.0 mol L^{-1} have sizes in the range of 79 ± 24 and 80 ± 23 nm, respectively. When the yields, phase compositions, morphology, and size are taken into account, we can conclude that the NaOH concentration at about 2.0 mol L^{-1} is the optimum for the formation of spherical $BaTiO_3$ nanoparticles in the present hydrothermal condition. The surfaces of the as-synthesized $BaTiO_3$ nanoparticles are smooth, and their sizes are uniform. In a high-concentration NaOH solution, the nuclei have a large amount of hydroxyl groups on their surfaces, which favor the growth of negatively charged $BaTiO_3$ nanoparticles at a pH ≥ 10 solution (Riman et al. 2002; Un-Yeon et al. 2004). The negatively charged $BaTiO_3$ nanoparticles can repel each other because of the electrostatic repulsion, which prevents them from agglomerating and enhances the dispersibility of the $BaTiO_3$ nanoparticles (Un-Yeon et al. 2004).

Figure 3g shows the plot of the yield of the solid samples as a function of NaOH concentrations [NaOH]. The yield is lower than 75 % when the [NaOH] concentration is in the range of 0.6–0.8 mol L^{-1}, whereas the yields increase to more than 90 % when the [NaOH] concentrations are larger than 1 mol L^{-1}.

Effects of molar Ba/Ti ratios

To verify the effect of the molar Ba/Ti ratios ($R_{Ba/Ti}$) on the formation of $BaTiO_3$ nanoparticles, we synthesized a series of $BaTiO_3$ samples by hydrothermal treatment of Ba^{2+}–TiO_2 sols with various Ba/Ti ratios ($R_{Ba/Ti} = 0.7$–2.0) and the optimal [NaOH] concentration of 2.0 mol L^{-1} at 200 °C for 10 h. Figure 4 shows the typical XRD patterns of the as-synthesized $BaTiO_3$ samples with various $R_{Ba/Ti}$ values. One can find that the diffraction peaks of all the samples obtained with $R_{Ba/Ti}$ of 0.7–2.0 can be readily attributed to cubic or tetragonal $BaTiO_3$ phases having

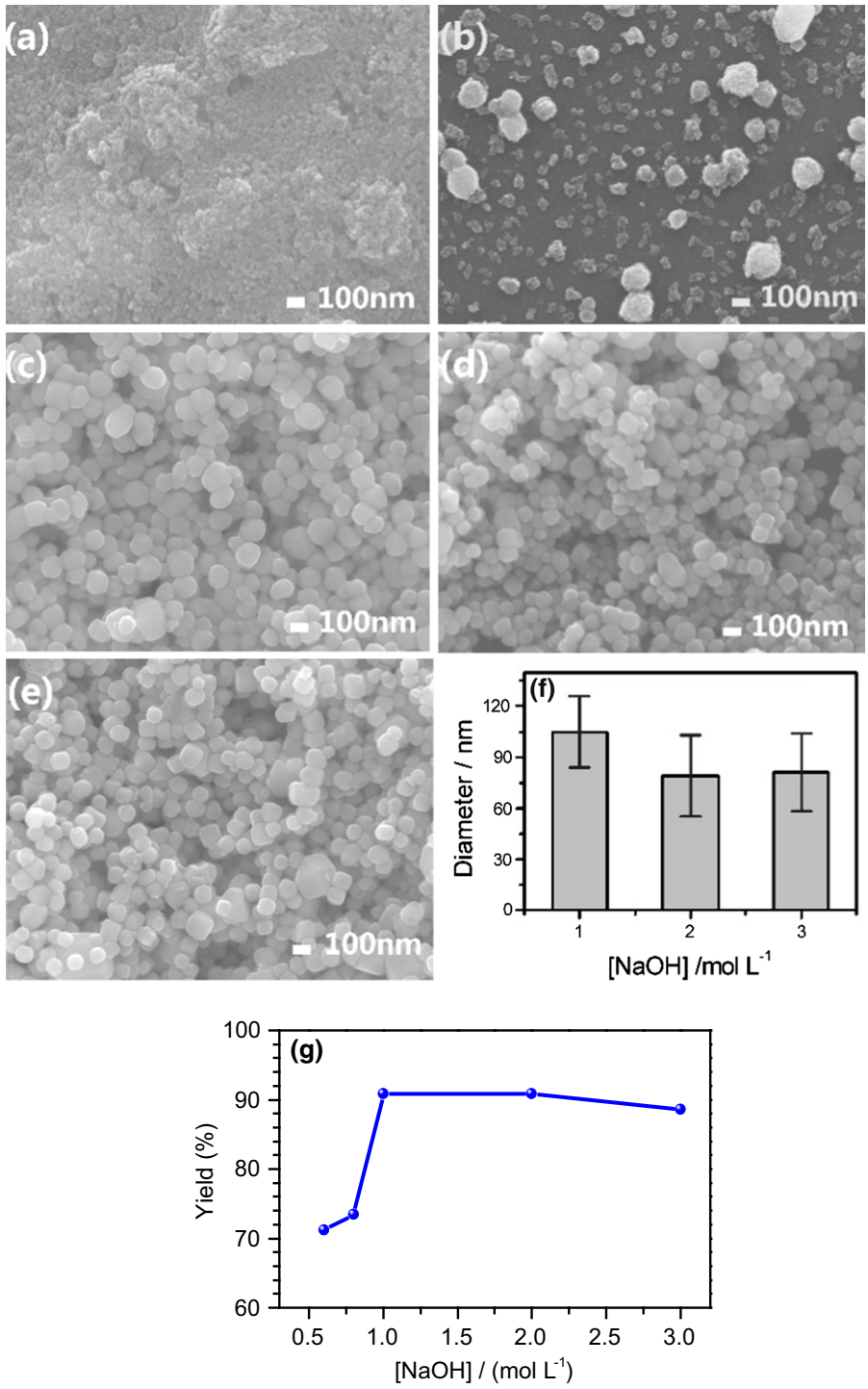

Fig. 3 **a–e** SEM images of $BaTiO_3$ samples obtained by static hydrothermal treatment at 200 °C for 10 h with $R_{Ba/Ti} = 1.2$ and various NaOH concentrations: **a** 0.6 mol L^{-1}, **b** 0.8 mol L^{-1}, **c** 1.0 mol L^{-1}, **d** 2.0 mol L^{-1}, and **e** 3.0 mol L^{-1}; **f** A histogram of the particle sizes changing with NaOH concentrations; **g** A plot of yields of the solid samples as a function of NaOH concentrations

no other recognizable impurities (Pramanik et al. 2006). The amplified XRD patterns in the 2θ range of 44–46° show that the peaks at around 45° become broader and broader as the $R_{Ba/Ti}$ value increases from 0.7 to 2.0, indicating a higher Ba/Ti ratio is helpful to form a tetragonal $BaTiO_3$ phase according to JCPDF

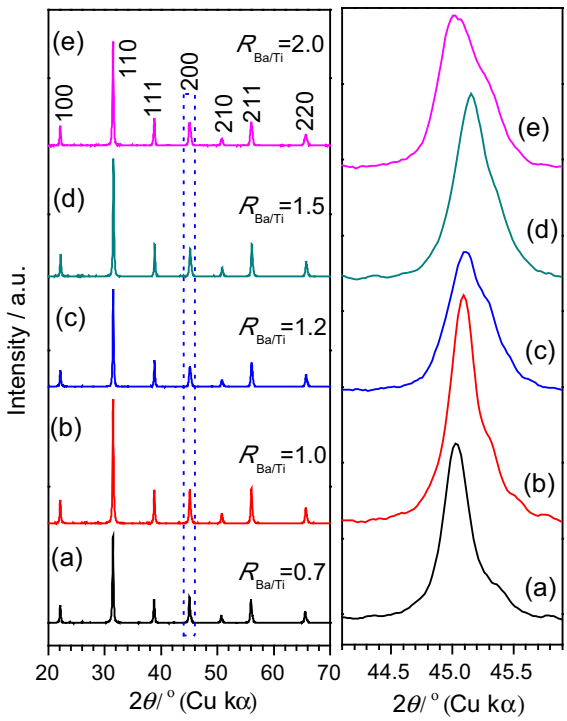

Fig. 4 Typical XRD patterns of $BaTiO_3$ samples obtained by static hydrothermal treatment at 200 °C for 10 h with [NaOH] = 2.0 mol L^{-1} and various molar Ba/Ti ratios ($R_{Ba/Ti}$): *a* $R_{Ba/Ti} = 0.7$, *b* $R_{Ba/Ti} = 1.0$, *c* $R_{Ba/Ti} = 1.2$, *d* $R_{Ba/Ti} = 1.5$, and *e* $R_{Ba/Ti} = 2.0$

no. 05-0626, in agreement with the literature results (Joung et al. 2011), but the proper Ba/Ti ratio is 1.2, larger than which the amount of tetragonal $BaTiO_3$ phase decreases (Table S1).

The morphology and particle-size distribution of the $BaTiO_3$ samples synthesized with various $R_{Ba/Ti}$ values via hydrothermal treatment at 200 °C for 10 h ([NaOH] = 2.0 mol L^{-1}) is shown in Fig. 5. Figure 5a–e shows the typical SEM images of the $BaTiO_3$ samples obtained, and their particle sizes analyzed based on the corresponding SEM observations are shown in Fig. 5f. One can find that the molar Ba/Ti ratios highly influence the morphologies of the $BaTiO_3$ samples. For the $BaTiO_3$ sample synthesized with a low $R_{Ba/Ti}$ value of 0.7, it consists of loose aggregates formed by small particles (Fig. 5a). The particle-like $BaTiO_3$ aggregates become tighter when the $R_{Ba/Ti}$ value increases to 1 (Fig. 5b). For the $BaTiO_3$ samples synthesized with $R_{Ba/Ti}$ values of 1.2 and 1.5, the particles have solid spherical shape with smooth surfaces (Fig. 5c–d). However, when the $R_{Ba/Ti}$ value continues to increase to 2.0 (Fig. 5e), the as-synthesized $BaTiO_3$ sample consists of large smooth particles (~100 nm) and small rough particles. The particle sizes of the samples slightly decrease as the $R_{Ba/Ti}$ value increases from 0.7 to 2.0 (Fig. 5f). It is obvious that a moderate $R_{Ba/Ti}$ value is favorable in forming uniform-sized $BaTiO_3$ nanospheres with smooth surfaces. Figure 5g shows the yield changes with the molar Ba/Ti ratios. One can find that the molar Ba/Ti ratios do not influence the yield of the solid samples very much, and their yields reach ~90 % for the $R_{Ba/Ti}$ values in the range of 0.7–2.0.

Effects of hydrothermal temperatures

We also investigated the effect of hydrothermal temperatures on the formation of $BaTiO_3$ nanocrystals when the other parameters were kept at optimal values: $R_{Ba/Ti} = 1.2$ and [NaOH] = 2.0 mol L^{-1}. Figure 6 shows the typical XRD patterns of the $BaTiO_3$ samples synthesized at various hydrothermal temperatures (100–200 °C) for 10 h. All the samples can be indexed to the $BaTiO_3$ phase (JCPDF no. 05-0626 and JCPDF no. 31-0174) (Masuda et al. 2008; Xie et al. 2010). The right part of Fig. 6 shows the reflection peaks at around 2θ of 45°. When the hydrothermal temperature enhances from 100 to 200 °C, the XRD peaks at around 2θ of 45° become broader, which indicates that the enhanced hydrothermal temperature is favorable in forming tetragonal $BaTiO_3$ phase. The percentages of tetragonal $BaTiO_3$ phase in the samples increase from 16.3 % at 100 °C to 36.6 % at 200 °C.

The SEM observations of the $BaTiO_3$ samples obtained at various temperatures are shown in Fig. 7. Figure 7a–d shows the typical SEM images of the $BaTiO_3$ samples synthesized at 100, 150, 180, and 200 °C, respectively. When the temperature is 100 °C, the as-obtained $BaTiO_3$ nanoparticles are of spherical shape and uniform size in morphology. With the increase in hydrothermal temperature, the $BaTiO_3$ particles show more definite crystal faces, indicating that higher temperature is more favorable in promoting the growth of $BaTiO_3$ nanoparticles (Fig. 7b–d). Figure 7e shows the particle-size change of the $BaTiO_3$ samples obtained at various hydrothermal temperatures. One can see that the elevated hydrothermal temperatures just slightly coarsen the $BaTiO_3$ particles from ~60 nm at 100 °C to ~80 nm at

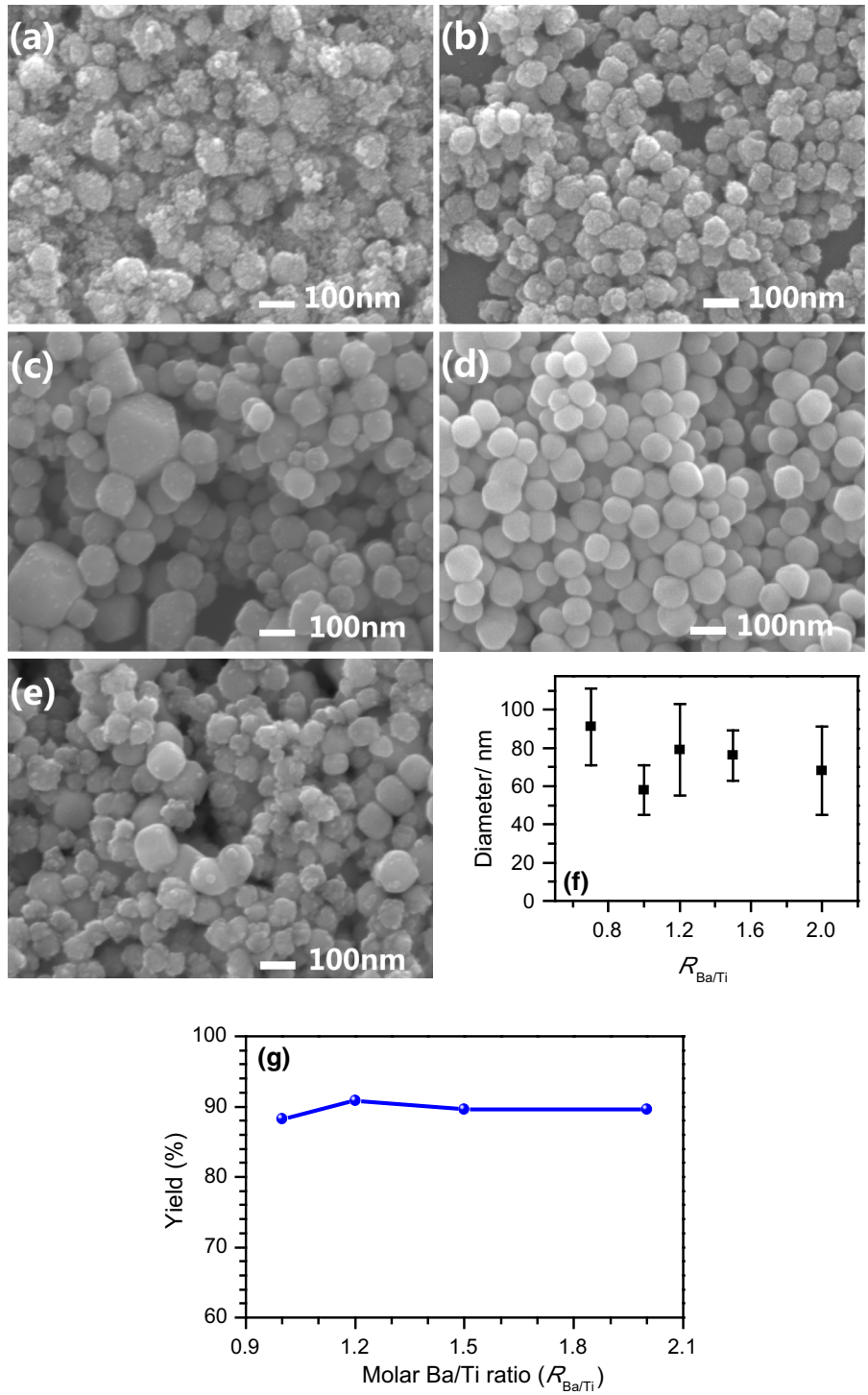

Fig. 5 **a–e** SEM images of $BaTiO_3$ samples obtained by static hydrothermal treatment at 200 °C for 10 h with [NaOH] = 2.0 -mol L^{-1} and various molar Ba/Ti ratios ($R_{Ba/Ti}$): **a** $R_{Ba/Ti} = 0.7$, **b** $R_{Ba/Ti} = 1.0$, **c** $R_{Ba/Ti} = 1.2$, **d** $R_{Ba/Ti} = 1.5$, and **e** $R_{Ba/Ti} = 2.0$; **f** The sizes of the $BaTiO_3$ samples changing with molar Ba/Ti ratios ($R_{Ba/Ti}$); **g** A plot of yields of the solid samples as a function of molar Ba/Ti ratios

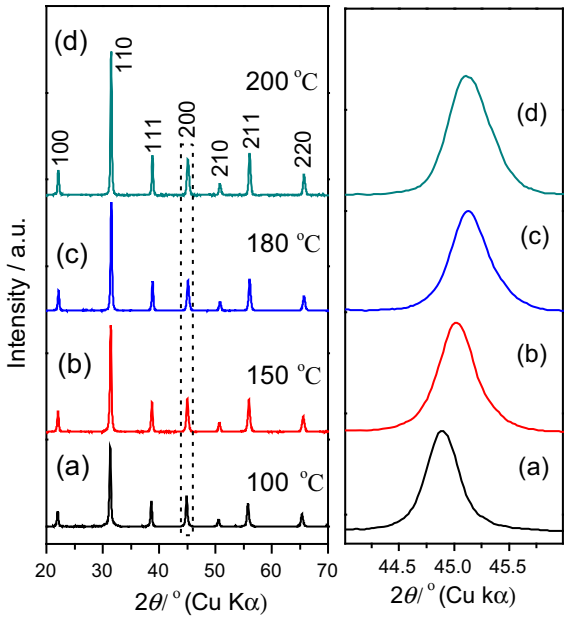

Fig. 6 Typical XRD patterns of $BaTiO_3$ samples by static hydrothermal treatment with $R_{Ba/Ti} = 1.2$ and [NaOH] = 2.0 mol L^{-1} at various temperatures for 10-h duration: *a* 100 °C, *b* 150 °C, *c* 180 °C and *d* 200 °C

200 °C. This insensitivity to hydrothermal temperature is useful in size-controllable synthesis of $BaTiO_3$ nanocrystals on a large scale. However, the hydrothermal temperatures highly influence the yields of the $BaTiO_3$ samples. Figure 7f shows the yields as a function of hydrothermal temperature. One can see that the elevated hydrothermal temperature can enhance the yields from ~88 % at 100 °C to ~92 % at 200 °C. Therefore, higher hydrothermal temperatures (i.e., 180–200 °C) are preferable in the high-yield synthesis of $BaTiO_3$ nanocrystals.

Growth mechanism of $BaTiO_3$ nanocrystals under static hydrothermal conditions

The investigation on the factors that influence the formation of $BaTiO_3$ nanoparticles indicates that the optimal parameters for the synthesis of uniform-sized $BaTiO_3$ nanospheres can be as follows: the $R_{Ba/Ti}$ values in a range of 1.2–1.5, the [NaOH] concentration is about 2.0 mol L^{-1}, and the hydrothermal temperature is in the range of 180–200 °C.

To explore the growth kinetics, we synthesized a series of $BaTiO_3$ samples with various hydrothermal durations (from 10 min to 100 h) under the above optimal conditions ($R_{Ba/Ti} = 1.2$, [NaOH] = 2.0 mol L^{-1}, at 200 °C). Figure 8 shows the typical XRD patterns of the $BaTiO_3$ samples synthesized with various hydrothermal durations. The overall XRD patterns in a 2θ range of 20–70° indicate the crystalline $BaTiO_3$ nanocrystals are formed after a hydrothermal treatment of 10 min, and the ignorable peak belonging to $BaCO_3$ phase suggests the $BaTiO_3$ samples are relatively pure even for the case with a hydrothermal duration as short as 10 min. The intensities of the XRD peaks become stronger and stronger as the hydrothermal durations increase from 10 min to 100 h. The crystalline sizes of the samples were estimated using the Scherrer equation, $D = K\lambda/\beta\cos\theta$, where $K = 0.89$, $\lambda = 0.15406$ nm, β is the FWHM of diffraction peak, and θ is diffraction angle. We calculated the crystalline sizes using the peaks at $2\theta = 22.1$, 31.5, 38.1°, respectively, and then averaged them. The diffraction peak intensities and the crystalline sizes increase when prolonging the hydrothermal treatment duration (Fig. S2), indicating that the increase of the XRD intensity is a direct consequence of the crystallite size growth. As the locally amplified XRD patterns in a 2θ range of 44–46° shows (right part of Fig. 8), there is only one typical peak at around 44.8° for the $BaTiO_3$ samples obtained at the initial stages (Fig. 8a–b), belonging to the (200) reflection of cubic $BaTiO_3$ phase (JCPDS card no. 31-0174)(Masuda et al. 2008; Patel et al. 2012). As the hydrothermal duration lengthens from 10 min to 100 h, the XRD peaks become stronger and stronger, and the diffraction peaks at around 45° broaden and finally split into two obvious peaks (Fig. 8g) at 44.9 and 45.3°, belonging to (200) and (002) reflections of tetragonal $BaTiO_3$ phase (JCPDS card no. 05-0626), respectively (Masuda et al. 2008; Patel et al. 2012; Joung et al. 2011; Xie et al. 2010). According to the XRD results, we can conclude that prolonging hydrothermal duration can promote the formation of tetragonal $BaTiO_3$ phase. We observed a great amount of tetragonal $BaTiO_3$ phase in the samples obtained after hydrothermal treatment for more than 5 h according to the XRD results (Fig. 8).

To further understand the growth process, we investigated the evolution in morphology and size of the $BaTiO_3$ samples obtained at various stages under the static hydrothermal conditions ($R_{Ba/Ti} = 1.2$, [NaOH] = 2.0 mol L^{-1}, at 200 °C). Figure 9 shows

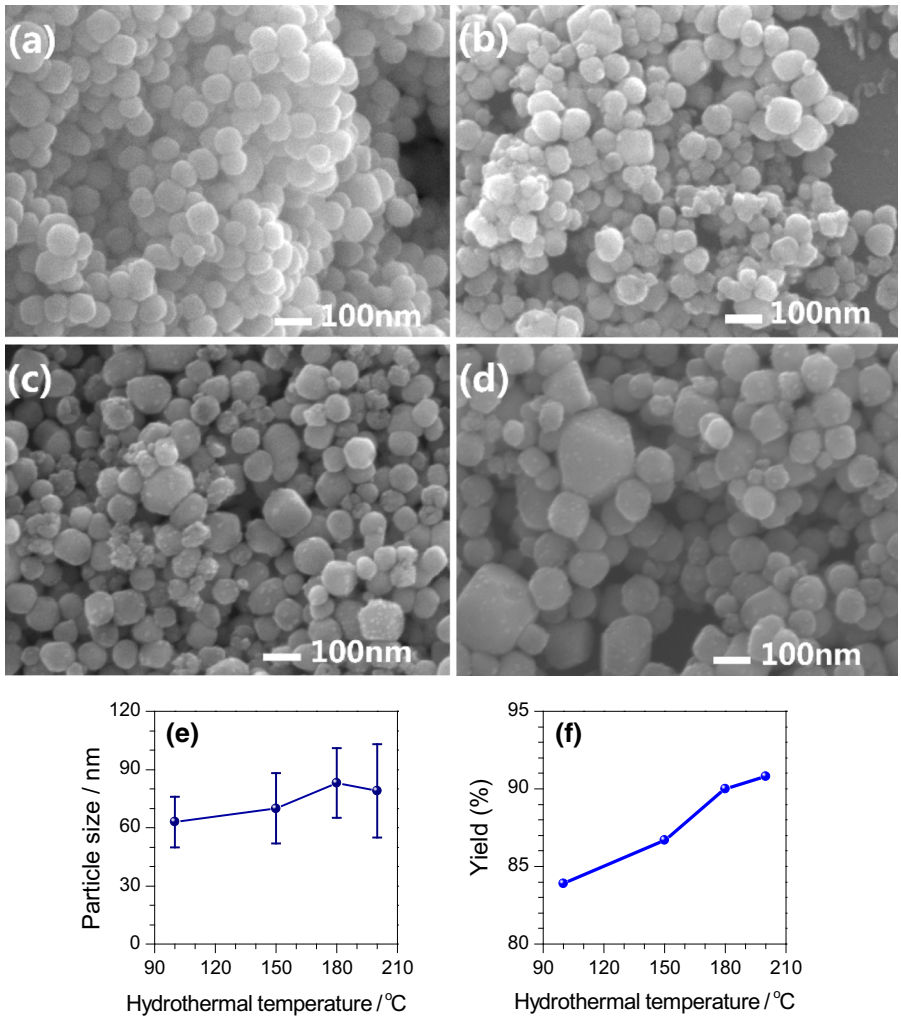

Fig. 7 **a–d** SEM images of $BaTiO_3$ samples by static hydrothermal treatment with $R_{Ba/Ti} = 1.2$ and [NaOH] = 2.0 mol L^{-1} at various temperatures for 10-h duration: **a** 100 °C, **b** 150 °C, **c** 180 °C and **d** 200 °C; **e** A plot of the sizes of the $BaTiO_3$ samples as a function of hydrothermal temperatures; **f** A plot of yields of the solid samples as a function of hydrothermal temperatures

the typical SEM observations (Fig. 9a–f) and statistical analyses in elemental compositions (Fig. 9g), particle-sizes (Fig. 9h) and yields (Fig. 9i). The typical SEM images in Fig. 9a–f show the evolution in morphology and size of the $BaTiO_3$ samples obtained with various hydrothermal durations from 10 min to 100 h. Figure 9a shows an SEM image of the solid sample at the very initial stage with a hydrothermal treatment of 10 min. One can see that it consists of small nanoparticles (several nanometers in size), which should be mainly TiO_2 nuclei. After a hydrothermal treatment of 60 min, uniform-sized spherical particles with a size range of 59 ± 13 nm are formed by agglomeration of smaller nanoparticles, as shown in Fig. 9b. As the hydrothermal duration increases from 1 to 100 h, the spherical $BaTiO_3$ particles become definitely plane-shaped polyhedral particles (Fig. 9c–f). Figure 9g shows the changes in the amounts of elemental Ba in the samples obtained with various hydrothermal durations based on the EDXA data. One can find that the Ba amount in the samples increases with the prolongation of hydrothermal duration, indicating that the elemental Ba enters $BaTiO_3$ lattices by gradually diffusing and growing

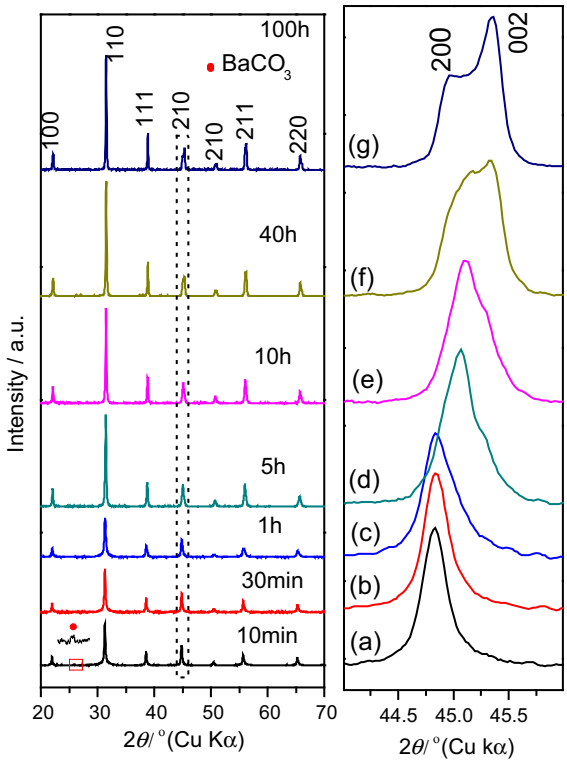

Fig. 8 Typical XRD patterns of $BaTiO_3$ nanoparticles synthesized with $R_{Ba/Ti} = 1.2$ and [NaOH] = 2.0 mol L^{-1} by hydrothermal treatment at 200 °C for various durations (10 min–100 h)

during the hydrothermal process. Figure 9h shows the particle-size changes of the samples synthesized at various stages, and their sizes increase gradually from 59 ± 13 to 147 ± 67 nm. Figure 9i shows the plot of the yields of the solid samples versus the hydrothermal duration. One can see that the yields of $BaTiO_3$ samples increase with the prolongation of the hydrothermal duration, and the yield shows a sharp increase during the initial hydrothermal stages.

To further understand the chemical compassions of the samples, we used TG–DTA and FT-IR techniques to characterize the typical samples obtained with various hydrothermal durations of 10 min, 10, and 100 h. According to the TG curves (Fig. S3a), the samples obtained with various hydrothermal durations of 10 min, 10, and 100 h exhibit total mass losses of ~11.3, 2.2, and 1.4 %, respectively. Their corresponding DTA curves (Fig. S3b) show that the sample obtained for a short hydrothermal duration of 10 min has an endothermic peak at 130 °C and an obvious exothermic peak at 200–500 °C, whereas these peaks become weaker for the samples obtained with longer hydrothermal durations of 10 h and 100 h. The endothermic peaks at 130 °C should be due to desorption of water and other impurities adsorbed on the samples (Patel et al. 2012). The exothermic peak and corresponding mass loss at 200–500 °C may be mainly due to the oxidation of the organic species derived from the precursor of tetrabutyl titanate (Patel et al. 2012).

We also used FT–IR spectra to characterize the samples prepared with various hydrothermal durations (Fig. S4). The bands at 3431 and 1568 cm^{-1} can be assigned to the (O–H)-stretching mode of the water molecules adsorbed (Long et al. 2011; Chang et al. 2009; Hou et al. 2009). The band at 2365 cm^{-1} may be due to some residual organic species. The band at 1400 cm^{-1} can be assigned to the (C=O) stretching mode (Long et al. 2011). These bands become weaker with the prolongation of the reaction duration. There are two obvious absorption bands in the wavenumber range of 400–800 cm^{-1}, which are similar to the literature (Long et al. 2011). The broad and strong absorption band at around 562 cm^{-1} can be assigned to Ti–O_I stretching normal vibrations of TiO_6 octahedra, and the weaker and sharper peak at around 438 cm^{-1} can be attributed to Ti–O_{II} bending normal vibrations (Zhan et al. 2012; Un-Yeon et al. 2004; Chang et al. 2009). These bands at 438 and 562 cm^{-1} become stronger and stronger when the hydrothermal duration increases from 10 h to 100 h, indicating the formation of well-crystallized $BaTiO_3$ nanocrystals. The FT-IR analysis agrees with the XRD results shown in Fig. 8.

To understand the growth mechanism, we use TEM technique to observe the typical $BaTiO_3$ samples obtained at the initial stages with hydrothermal durations of 10 min and 1 h. The low-magnification TEM images (Fig. S5) indicate that these samples consist of highly dispersive spherical particles with sizes of 50-60 nm, similar to the SEM observations (Fig. 9). The enlarged TEM images and the corresponding fast Fourier transform (FFT) patterns are shown in Fig. 10. The TEM images in Fig. 10a and d show that the spherical particles in the samples take on a roughly surface, and their high-resolution TEM images (Fig. 10b and e) indicate that the spherical particles are formed by loosely aggregating smaller nanoparticles (5–10 nm in size). One can see some

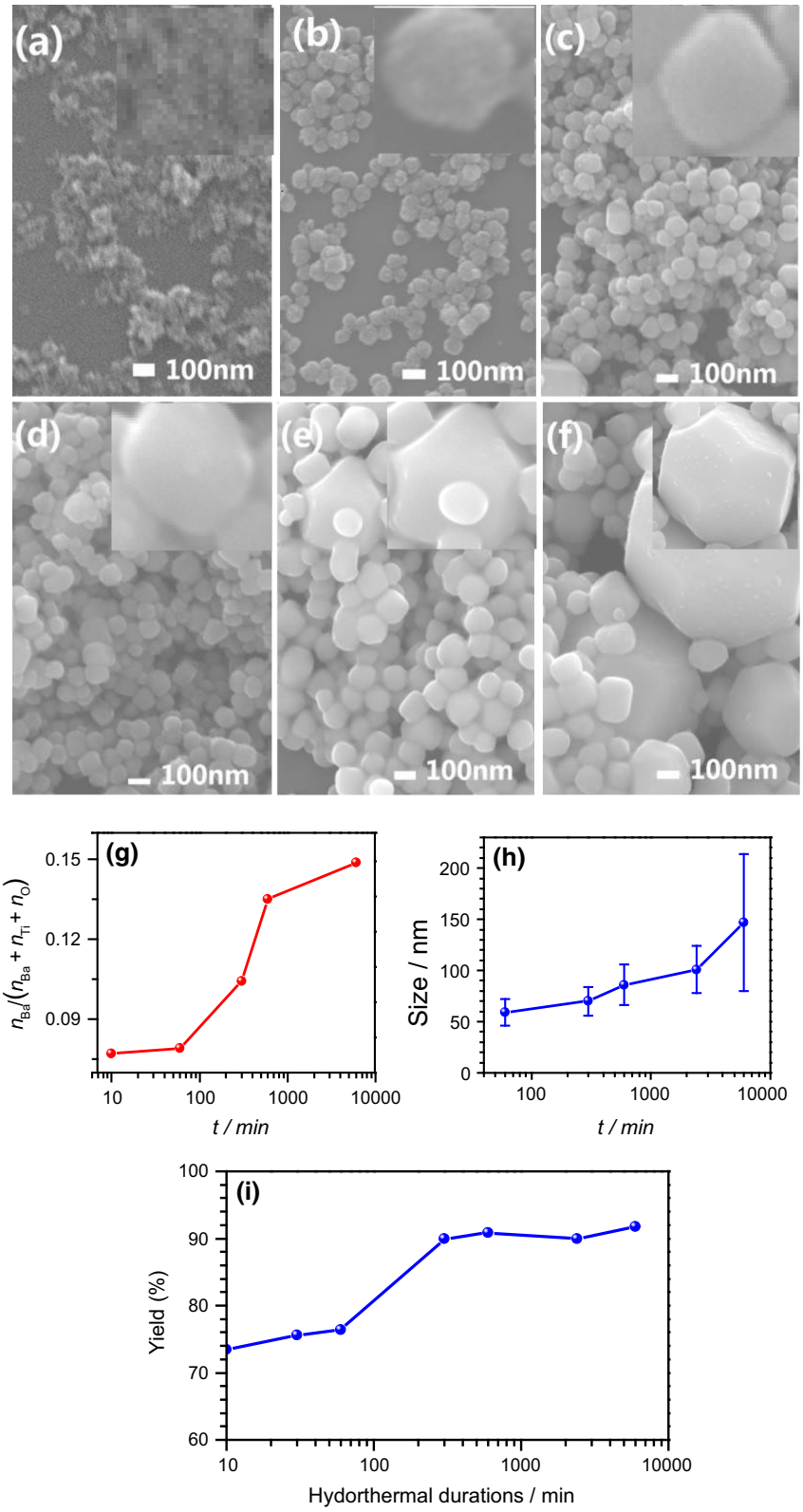

Fig. 9 **a–f** SEM images of the $BaTiO_3$ nanocrystals synthesized with $R_{Ba/Ti} = 1.2$ and $[NaOH] = 2.0$ mol L^{-1} by hydrothermal treatment at 200 °C for 10 min–100 h: **a** 10 min, **b** 1 h, **c** 5 h, **d** 10 h, **e** 40 h, **f** 100 h; **g** The change of the Ba amount of the $BaTiO_3$ nanocrystals obtained with various hydrothermal durations according to the EDXA data; **h** The changes in the sizes of the $BaTiO_3$ nanocrystals obtained with various hydrothermal durations according to the SEM observation; **i** A plot of yields of the solid samples as a function of hydrothermal durations

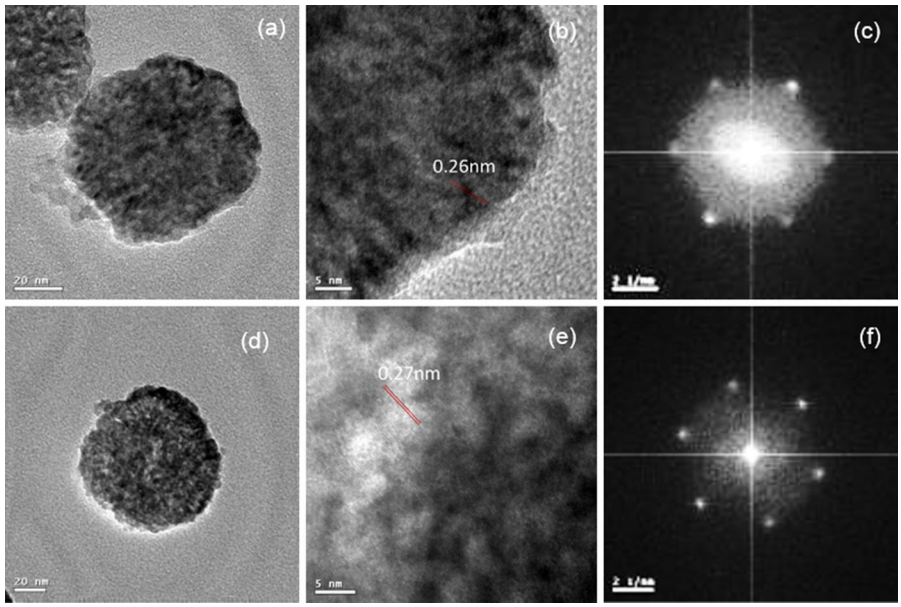

Fig. 10 **a**, **b**, **d**, **e** TEM images and **c**, **f** FFT patters of the $BaTiO_3$ nanocrystals obtained by hydrothermal treatment with $R_{Ba/Ti} = 1.2$, [NaOH] = 2.0 mol L^{-1} at 200 °C for **a**–**c** 10-min and **d**–**f** 1-h durations

well-defined lattice fringes in the high-resolution TEM images, and the spacings of the lattice fringes are about 0.26 and 0.27 nm, which correspond to the {110} crystal planes of cubic $BaTiO_3$. The corresponding FFT patterns in Fig. 10 c and f show ordered diffractional lattices, which can be indexed to the cubic $BaTiO_3$ phase along the [111] direction. Taking the SEM, TEM, and FFT results into consideration, we can safely conclude that the nanoparticles are aggregated via an oriented attachment mechanism to form larger spherical particles at the initial stages during the hydrothermal process.

The growth mechanism of the $BaTiO_3$ nanocrystals during the static hydrothermal conditions can be understood based on the analyses of the XRD, SEM, TEM, TG–DTA, and FT-IR results. Figure 11 shows the schematic process for the possible growth mechanism of the $BaTiO_3$ nanoparticles. At the initial stage of crystal growth, there is a competition between the aggregation and growth processes. The crystal growth of $BaTiO_3$ nanocrystals under static hydrothermal conditions can be divided into three distinct stages according to their morphologic evolution (Fig. 9): nucleation, fast aggregation, and Ostwald ripening growth. During the nucleation stage, the Ti–O chains with negative charge were quickly formed under the strong alkali solution, and then adsorbed the positive-charged Ba^{2+} ions, followed by nucleation and crystallization to form $BaTiO_3$ nuclei with small particle sizes (Figs. 8a, 9a). At the second stage, the newly formed $BaTiO_3$ nuclei aggregate to form spherical particles with a uniform size (Figs. 9b, 10, Fig. S5). Usually, the $BaTiO_3$ nanoparticles with similar distances will take the same crystallographic orientation because of the induction effect of the large crystals with a direction of polarization to the small ones (Chang et al. 2009). The loose and oriented $BaTiO_3$ aggregates then in situ crystallize during the hydrothermal conditions. The particle sizes and the morphology of $BaTiO_3$ nanocrystals have not undergone obvious changes during the orientated aggregation and crystallization stage, as shown in Fig. 9c, d. When the hydrothermal duration is further extended, the Ostwald ripening mechanism will become dominant during the growth of $BaTiO_3$ nanocrystals (Zeng 2007). During the Ostwald ripening process, smaller grains with greater solubility dissolve and grow on the larger grains with smaller solubility, making the larger grains grow further and the small grains disappear (Fig. 9e, f), and the particle size-distribution range will broaden as the hydrothermal duration increases (Fig. 9h) (Zeng 2007; Ma et al. 1997). Therefore,

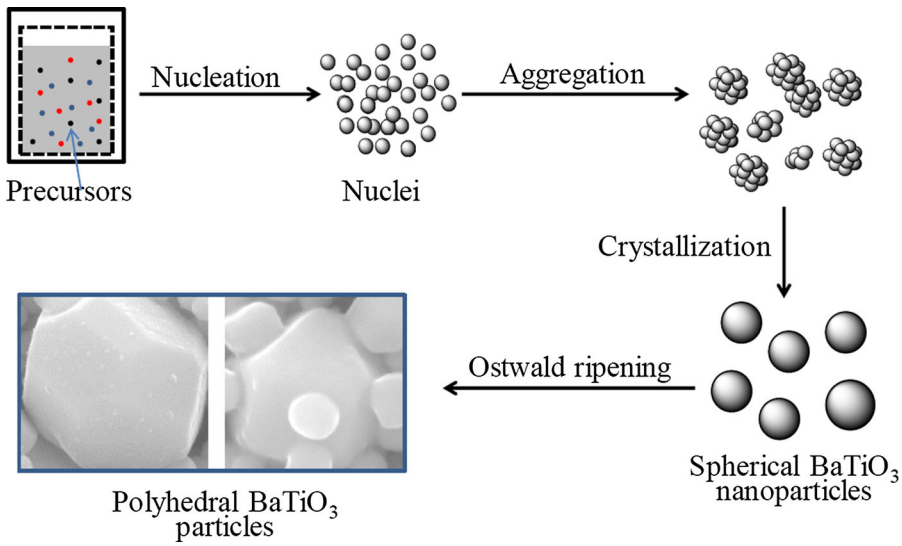

Fig. 11 A schematic demonstration for the growth mechanism of $BaTiO_3$ nanocrystals under the static hydrothermal process

determining a proper hydrothermal duration is very important for the formation of spherical $BaTiO_3$ nanocrystals with uniform size and morphology.

Conclusions

We have systematically investigated the factors that influence the formation of $BaTiO_3$ nanocrystals during the static hydrothermal process, and highly dispersed $BaTiO_3$ nanospheres (76 ± 13 nm) with uniform size and morphology have been synthesized under the optimal conditions. The effects of NaOH concentrations ([NaOH], 0.6–3.0 mol L^{-1}), molar Ba/Ti ratios ($R_{Ba/Ti}$, 0.7–2.0), hydrothermal temperatures (100–200 °C), and durations (10 min–100 h) on the formation of $BaTiO_3$ nanocrystals have been investigated, with an emphasis on understanding the related formation mechanisms. The sizes and morphology of $BaTiO_3$ nanoparticles can be controlled by changing NaOH concentrations, the Ba/Ti ratio, and hydrothermal temperatures, and durations. The results indicate that higher NaOH concentrations, higher Ba/Ti ratios, higher hydrothermal temperatures, and longer hydrothermal durations are favorable in forming $BaTiO_3$ nanocrystals with a larger fraction of tetragonal phase. The optimal parameters of [NaOH] = 2.0 mol L^{-1} and $R_{Ba/Ti} = 1.5$ at the hydrothermal temperature of 200 °C for 10 h can synthesize highly dispersed $BaTiO_3$ nanocrystals with uniform size and spherical morphology. The formation of $BaTiO_3$ nanocrystals under the static hydrothermal conditions experience three stages at least: (i) nucleation of small $BaTiO_3$ nuclei, (ii) rapid aggregation and in situ crystallization to form spherical $BaTiO_3$ nanoparticles, and (iii) formation of polyhedral $BaTiO_3$ particles via an Oswald ripening process. This work provides further understanding on how to synthesize highly dispersed $BaTiO_3$ nanoparticles with uniform morphology for important applications in functional micro/nanoscale devices fabricated by ink-jet printing techniques.

Acknowledgments This work was partly sponsored by the National Natural Science Foundation of China (51172211, 512101207, 51172213), China Postdoctoral Science Foundation (2013M531682, 2014T70682), the Foundation for University Young Key Teacher by Henan Province (2011GGJS-001), the Program for Science&Technology Innovation Talents in Universities of Henan Province (14HASTIT011), and the Special Support Program For High-End Talents of Zhengzhou University (ZDGD13001).

References

Badheka P, Qi L, Lee BI (2006) Phase transition in barium titanate nanocrystals by chemical treatment. J Eur Ceram Soc 26(8):1393–1400

Bai Y, Ding K, Zheng GP (2012) Entropy-change measurement of electrocaloric effect of $BaTiO_3$ single crystal. Phys Status Solidi A 209(5):941–944

Bandura AV, Evarestov RE (2012) First-principles calculations on thermodynamic properties of $BaTiO_3$ rhombohedral phase. J Comput Chem 33(18):1554–1563

Chang SJ, Liao WS, Chou CJ (2009) An efficient approach to derive hydroxyl groups on the surface of barium titanate nanoparticles to improve its chemical modification ability. J Colloid Interface Sci 329:300–305

Gajović A, Pleština JV, Žagar K (2013) Temperature-dependent Raman spectroscopy of $BaTiO_3$ nanorods synthesized by using a template-assisted sol-gel procedure. J Raman Spectrosc 44:412–4120

Haertling GH (1999) Ferroelectric ceramics: history and technology. J Am Ceram Soc 4:797–818

Hoshina T, Wada S, Kuroiwa Y, Tsurumi T (2008) Composite structure and size effect of barium titanate nanoparticles. Appl Phys Lett 93:192914–192918

Hou RZ, Ferreira P, Vilarinho PM (2009) Nanoporous $BaTiO_3$ crystallites. Chem Mater 21(15):3536–3541

Hwang KS, Song JE, Jo JW, Yang HS (2002) Effect of poling conditions on growth of calcium phosphate crystal in ferroelectric $BaTiO_3$ ceramicsa. J Mater Sci 13:133–138

Joung MR, Kim JS, Song ME (2011) Synthesis of highly tetragonal $BaTiO_3$ nanopowders by a two-step alkoxide–hydroxide route. J Alloy Compd 509(37):9089–9092

Kim YH, Kook K, Hwang SK (2014) Polymer/perovskite-type nanoparticle multilayers with multielectric properties prepared from ligand addition-induced layer-by-layer assembly. ACS Nano 8(3):241–249

Kimmel AV, Íñiguez J, Cain MG, Sushko PV (2013) Neutral and charged oxygen vacancies induce two-dimensional electron gas near $SiO_2/BaTiO_3$. J Phys Chem Lett 4:333–337

Ko YN, Choi SH, Kang YC (2013) Nano-sized Ag-$BaTiO_3$ composite powders with various amount of Ag prepared by spray pyrolysis. J Eur Ceram 33(7):1335–1341

Koka A, Sodano HA (2013) High-sensitivity accelerometer composed of ultra-long vertically aligned barium titanate nanowire arrays. Nat Commun 4:2682–2686

Long X, Ma YR, Qi LM (2011) In vitro synthesis of high Mg calcite under ambient conditions and its implication for biomineralization process. Cryst Growth Des 11:2866–2873

Ma Y, Vileno E, Suib SL (1997) Synthesis of tetragonal $BaTiO_3$ by microwave heating and conventional heating. Chem Mater 9:3023–3031

Masuda Y, Koumura T, Okawa T, Koumoto K (2003) Micropatterning of Ni particles on a $BaTiO_3$ green sheet using a self-assembled monolayer. J Colloid Interface Sci 263:190–1995

Masuda Y, Yamada T, Koumoto K (2008) Synthesis of acicular $BaTiO_3$ particles using acicular barium oxalates. Cryst Growth Des 8(1):169–171

Moreira ML, Microwave H (2008) Hydrothermal microwave: a new route to obtain photoluminescent crystalline $BaTiO_3$ nanoparticles. Chem Mater 20:5381–5387

Ouyang J, Yang HM, He X, Liu H (2010) Novel preparation and characterization of barium strontium titanate microcubes. J Am Ceram Soc 93:3342–3348

Paniagua SA, Kim YS, Henry K (2014) Surface-Initiated polymerization from barium titanate nanoparticles for hybrid dielectric capacitors. ACS Appl Mater Interfaces 6:3477–3482

Patel S, Kumar RK, Prakash P, Agrawal C (2012) Low temperature synthesis and dielectric, ferroelectric and piezoelectric study of microwave sintered $BaTiO_3$ ceramics. Ceram Int 38(2):1585–1589

Pramanik NC, Seok S, Ahn BY (2006) Wet-chemical synthesis of crystalline $BaTiO_3$ from stable chelated titanium complex: Formation mechanism and dispersibility in organic solvents. J Colloid Interface Sci 300:569–576

Qi JQ, Peng T, Hu YM (2011) Direct synthesis of ultrafine tetragonal $BaTiO_3$ nanoparticles at room temperature. Nanoscale Res Lett 6(4):466–470

Riman RE, Suchanek WL, Lencka MM (2002) Hydrothermal crystallization of ceramics. Ann Chim Sci Mat 27(6):15–36

Sahonta FT, Garcia SL, Driscoll VM (2011) Structural and dielectric properties of $SnTiO_3$, a futative ferroelectric. Cryst Growth Des 5:1422–1426

Shin SH, Kim YH, Lee MH (2014) Hemispherically aggregated $BaTiO_3$ nanoparticle composite thin film for high-performance flexible piezoelectric nanogenerator. ACS Nano 8(3):2766–2773

Shiratori Y, Pithan C, Dornseiffer J, Waser R (2007) Raman scattering studies on nanocrystalline $BaTiO_3$ Part I-isolated particles and aggregates. J Raman Spectrosc 38:1288–1299

Slamovich EB, Aksay I (1994) Hydrothermal procession of $BaTiO_3$/polymer films. Mat Res Soc Symp Proc 346:63–68

Stawski TM, Veldhuis SA, Besselink R (2012) Nanoscale structure evolution in alkoxide–carboxylate Sol-Gel precursor solutions of barium titanate. J Phys Chem C 116:425–434

Szwarcman D, Vestler D, Markovich G (2011) The size-dependent ferroelectric phase transition in $BaTiO_3$ nanocrystals probed by surface plasmons. ACS Nano 5:507–515

Tang HX, Sodano HA (2013) Ultra high energy density nanocomposite capacitors with fast discharge using $Ba_{0.2}$-$Sr_{0.8}TiO_3$nanowires. Nano Lett 13:1373–1379

Tian XL, Li J, Chen K (2008) Template-free and scalable synthesis of core-shell and hollow $BaTiO_3$ particles: using molten hydrated salt as a solvent. Cryst Growth Des 9(11):3309–3333

Un-Yeon H, Hyung-Sang P, Kee-Kahb K (2004) Low-temperature synthesis of fully crystallized spherical $BaTiO_3$ particles by the Gel-Sol method. J Am Ceram Soc 87(12):2168–2174

Wang XY, Lee BI, Hu M, Payzant EA, Blom DA (2006) Nanocrystalline $BaTiO_3$ powder via a sol process ambient conditions. J Eur Ceram Soc 26(12):2319–2326

Xia CT, Shi EW, Cryst Zhong WZ (1996) Hydrothermal synthesis of $BaTiO_3$ nano/microcrystals. J Cryst Growth 166:961–966

Xie YH, Yin S, Hashimoto T (2010) Low temperature synthesis of tetragonal $BaTiO_3$ by a novel composite-hydroxide-mediated approach and its dielectric properties. J Eur Ceram Soc 30(3):699–704

Xu HR, Gao L (2002) New evidence of a dissolution–precipitation mechanism in hydrothermal synthesis of barium titanate powders. Mater Lett 57:490–494

Zeng HC (2006) Synthetic architecture of interior space for inorganic nanostructures Chem. J Mater Chem 16(7):649–656

Zeng HC (2007) Ostwald ripening: a synthetic approach for hollow nanomaterials. Curr Nanosci 3:177–1781

Zhan HQ, Yang XF, Wang CM (2012) Multiple nucleation and crystal growth of barium titanate. Cryst Growth Des 12(3):1247–1253

Zhou WZ (2010) Reversed crystal growth: implications for crystal engineering. Adv Mater 22(28):3086–3092